

博士論文（要約）

Exploration of high-voltage cathode materials based on cationic and anionic redox chemistry

（カチオンおよびアニオンの酸化還元化学に基づく高電圧正極材料の開発）

川合 航右

1. General introduction

Establishing a sustainable society requires electrical energy storages as a ubiquitous technology. Nowadays, lithium-ion battery (LIB) dominates the global battery market owing to high performances such as high energy density and long cycle life. However, extensive deployments of grid energy storages and electric vehicles demand further improvements of material cost and energy density. In this thesis, exploration of cathode materials is conducted to eliminate these bottlenecks.

2. High-voltage $\text{Cr}^{4+}/\text{Cr}^{3+}$ redox couple in phosphate-based compounds

Sodium-ion batterie (SIB) is a promising alternative for LIB because sodium resources are more abundant and widely distributed in the earth than lithium. However, higher redox potential of Na/Na^+ than that of Li/Li^+ by 0.3 V leads to lower operating voltages of SIBs than that of LIBs. Overcoming this disadvantage needs development of high-voltage cathode materials for SIBs. Phosphate-based compounds are practical candidates because of the high chemical and thermal stability, and the moderate inductive effect of phosphate ion.^{1,2} Typical designs of high-voltage phosphate-based cathodes rely on high-cost cobalt or nickel, which exhibit redox reactions above 4.0 V vs. Na/Na^+ .^{3,4} In contrast, low-cost chromium-based phosphates are predicted to show an operating voltage at 4.9 V vs. Li/Li^+ using $\text{Cr}^{4+}/\text{Cr}^{3+}$ redox couple.⁵ Indeed, anti-NASICON $\text{Li}_3\text{Cr}_2(\text{PO}_4)_3$ exhibits electrochemical Li^+ extraction at 4.8 V vs. Li/Li^+ , whereas the experimental verification of $\text{Cr}^{4+}/\text{Cr}^{3+}$ redox reaction has been limited.⁶ Herein, electrochemical activities of chromium-based phosphates are investigated to develop high-voltage cathode materials.

NASICON-type $\text{Na}_3\text{Cr}_2(\text{PO}_4)_3$ exhibits an electrochemical activity at 4.5 V vs. Na/Na^+ with a reversible capacity of 80.2 mAh/g, which corresponds to 1.4 electron reaction per formula unit (Fig. 1). *Ex situ* powder X-ray diffraction (XRD) measurement demonstrates the biphasic structural transition during the first cycle although structural degradation is observed after 20th cycle.

To realize a stable $\text{Cr}^{4+}/\text{Cr}^{3+}$ redox reaction in phosphates, ion-substitution for Cr^{3+} with d^0 transition-metal ions was conducted to alleviate the structural distortions upon Na^+ (de)intercalation: d^0 cations, for example, Ti^{4+} , V^{5+} , Nb^{5+} , and Ta^{5+} , allow out-of-center distortions by the second-order Jahn–Teller effect.^{7,8} NASICON-type $\text{Na}_2\text{CrTi}(\text{PO}_4)_3$ shows a reversible capacity for the first cycle (43.7 mAh/g) and a capacity retention of 90% with no voltage decay after 50th cycle (Fig. 2). Rietveld refinement of XRD pattern for fully charged state suggests a composition of $\text{NaCrTi}(\text{PO}_4)_3$. Cr $L_{2,3}$ -edge X-ray absorption spectroscopy (XAS) measurements detect the core electron excitation ($2p^63d^2 \rightarrow 2p^53d^3\bar{L}$, \bar{L} : ligand hole), which is typical for compounds containing Cr^{4+} (Fig. 3).⁹ These results indicate that the full $\text{Cr}^{4+}/\text{Cr}^{3+}$ redox reaction with Na^+ (de)intercalation occurs as follows:



In situ XRD measurement during the first cycle demonstrates that the Na^+ (de)intercalation reaction entails continuous shifts of the Bragg positions, reflecting a monophasic structure evolution with a continuous lattice volume change. A possible

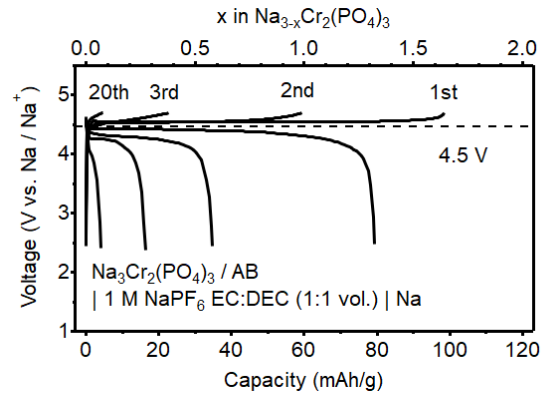


Fig. 1 Galvanostatic charge/discharge curves of $\text{Na}_3\text{Cr}_2(\text{PO}_4)_3$ electrode.

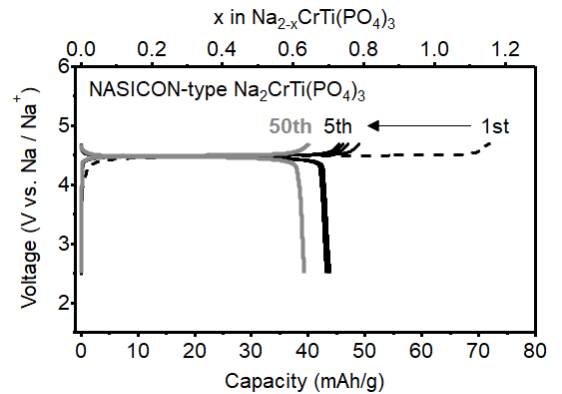


Fig. 2 Galvanostatic charge/discharge curves of $\text{Na}_2\text{CrTi}(\text{PO}_4)_3$ electrode in SIB. Inset shows Ti-substitution dependence of cycle performance.

explanation for the increasing capacity retention by Ti-substitution is that the small biphasic miscibility gap over a wide Na-composition range mitigates interfacial stresses on the biphasic boundary during the electrode reactions.

For further exploration of chromium-based phosphate cathodes, an electrochemical activity of $\text{Na}_3\text{Cr}_2(\text{PO}_4)_2\text{F}_3$ is investigated. $\text{Na}_3\text{Cr}_2(\text{PO}_4)_2\text{F}_3$ delivers a reversible capacity of 55.1 mAh/g equivalent to 0.86 Na^+ intercalation per formula at 4.7 V vs. Na/Na^+ (Fig. 4). The increase of operating voltage from that of $\text{Na}_{3-y}\text{Cr}_{2-y}\text{Ti}_y(\text{PO}_4)_3$ is likely due to localization of valence electron on Cr 3d state through incorporating more electronegative F^- than PO_4^{3-} into the polyanion framework. Cr $L_{2,3}$ -edge and O K -edge XAS spectrum confirms the charge compensation using $\text{Cr}^{4+}/\text{Cr}^{3+}$ redox couple and the creation/annihilation of ligand hole on oxygen upon Na^+ (de)intercalation. Density functional theory (DFT) calculations support this mechanism: antibonding Cr 3d–O 2p state near the Fermi level possesses the uniform charge distribution on chromium and oxygen atoms before and after Na^+ extraction (Fig. 5).

Fig. 6 shows a schematic derivation of the operating voltages and d -band positions of 3d transition-metal phosphates in sodium-ion batteries. In general, the depth of the 3d energy levels is dominated by the nuclear charge and valence number. Transition-metal ions M^{n+} with larger atomic numbers have deeper valence levels owing to their greater nuclear charge, resulting in a higher $M^{(n+1)+}/M^{n+}$ redox potential. A larger oxidation number (n) also results in a higher redox potential. Naturally, phosphates with late transition metals such as $\text{Co}^{3+}/\text{Co}^{2+}(d^6/d^7)$ and $\text{Ni}^{3+}/\text{Ni}^{2+}(d^7/d^8)$ have been investigated for high-voltage operation. However, a large number of d -electrons (>5) in late transition metals suffer from energy-level increments by experiencing intra-orbital Coulombic penalties and/or crystal field splitting. On the other hand, the early transition metals Cr functions at competitively high voltages (>4 V) with higher oxidation numbers, $M^{4+}/M^{3+}(d^2/d^3)$, where less than half-filled (≤ 3) highest energy levels composed of t_{2g} orbitals are free from the energy penalty, either by intra-orbital Coulombic repulsion or crystal field splitting. This situation, combined with the introduction of electronegative F^- ions, yields a record high-voltage in early 3d transition metal-based cathodes in $\text{Na}_{3-y}\text{CrTi}(\text{PO}_4)_3$ and $\text{Na}_{3-x}\text{Cr}_2(\text{PO}_4)_2\text{F}_3$ (4.5 and 4.7 V vs. Na/Na^+ , respectively), even with inherently higher d -electron energy levels owing to smaller nuclear charge.

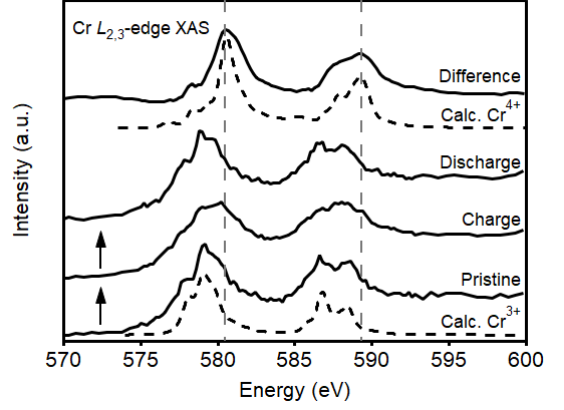


Fig. 3 *Ex situ* Cr $L_{2,3}$ -edge and O K -edge XAS of $\text{Na}_{2-x}\text{CrTi}(\text{PO}_4)_3$ electrodes.

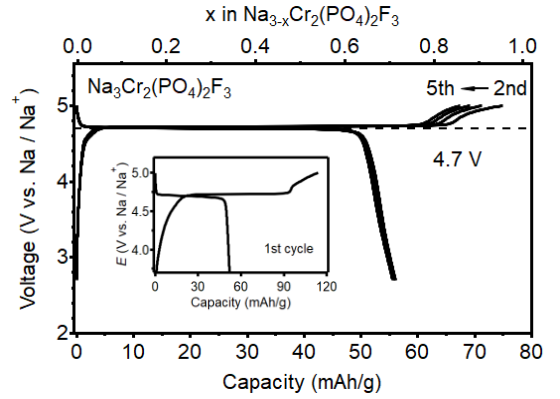


Fig. 4 Galvanostatic charge/discharge curves of $\text{Na}_{3-x}\text{Cr}_2(\text{PO}_4)_2\text{F}_3$ electrode in 2.7–5.0 V vs. Na/Na^+ . An inset shows 1st cycle with a large irreversible capacity.

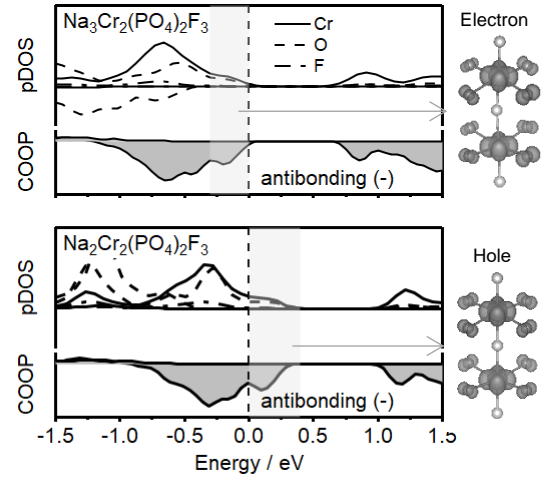


Fig. 5 Calculated projected density of states (pDOS) and Cr–O crystal orbital overlap population (COOP).

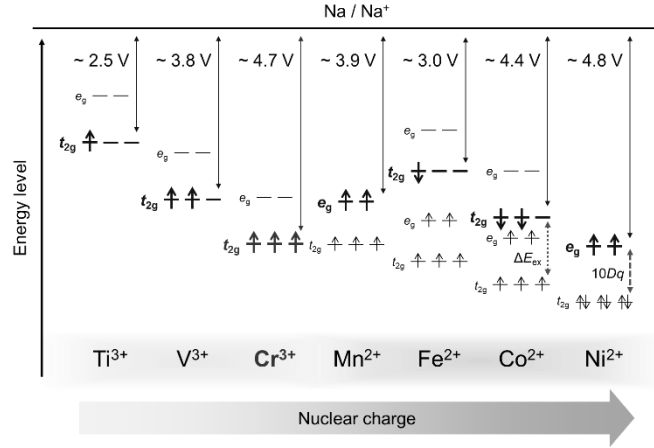
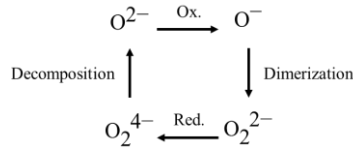


Fig. 6 Comparison of operating voltages and valence states of phosphate-based cathode materials.

3. Kinetic peroxide formation for voltage hysteresis of oxygen-redox battery electrodes

Conventional cathode materials, *i.e.*, layered transition-metal oxides O3-type LiMO₂ (*M* = transition metal, O3: lithium ions occupy octahedral sites between MO₂ layers and the packing of oxide ions is ABCABC), deliver a modest capacity of *ca.* 150 mAh/g using cationic redox reactions. In contrast, recent intensive research has demonstrated that lithium-rich transition-metal oxides (Li_{1+x}M_{1-x}O₂) exhibit large capacities (>200 mAh/g) through activating additional redox reactions of oxide ions.^{10,11} However, a large voltage hysteresis (>0.8 V) of the charge/discharge process reduces energy density and energy efficiency, which is a bottleneck for practical use of oxygen-redox cathodes. The hypothetical mechanism of oxygen-redox reactions is described as a square scheme:



where unstable O^{·-} radicals dimerize to form stable peroxide ion O₂²⁻ during charge, while an unstable reduced dimer (*e.g.*, O₂⁴⁻) decomposes to O²⁻ during discharge.^{12,13} This mechanism seems plausible based on fragmental experimental observations such as the large voltage hysteresis and spectroscopic O₂²⁻ detection after charge.¹⁴ However, the structural degradation of O3-type oxides, *e.g.*, layered-to-spinel transformation and surface cation densification upon cycling (Fig. 7a),^{13,15} complicates experimental investigation for the square scheme.

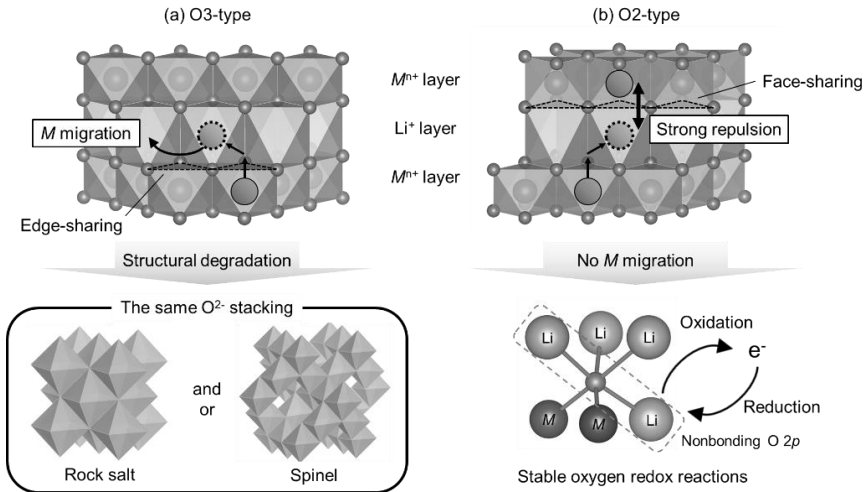


Fig. 7 The migration path of a transition-metal (*M*) cation into an adjacent lithium layer in (a) O3 and (b) O2-type layered oxides.

Recent studies have demonstrated the structural integrity of O2-type layered oxides (O2: lithium ions occupy octahedral sites between MO_2 layers and the packing of oxide ions is ABCBA) against the degradation upon oxygen-redox reactions: M migration to Li^+ layers is unfavorable because M in a Li^+ layer suffers from strong Coulombic repulsion from M^{n+} in an adjacent MO_2 layer (Fig. 7b).^{16,17} Herein, O_2^{2-} formation in O2-type $Li_{1.12-y}Ni_{0.17}Mn_{0.71}O_2$ is elucidated by using experimental and computational analysis. Furthermore, a rate constant of the dimerization reaction in oxygen-redox electrodes is calculated based on a simple model for the kinetic formation of O–O bond.

$O_2-Li_{1.12-y}Ni_{0.17}Mn_{0.71}O_2$ delivers a large specific capacity of *ca.* 210 mAh/g, exceeding a M -redox capacity (193 mAh/g). 99.4% of the discharge capacity was retained after 80 cycles and decay of the average discharge voltage is negligible (<6 mV) (Fig. 8a). The dQ/dV plots of charge/discharge curves with incremental upper cutoff voltages from 2.9 to 4.8 V vs. Li/Li^+ show the polarizing reduction peak at 3.3 V vs.

Li/Li^+ after charging above 4.2 vs. Li/Li^+ as well as the nonpolarizing redox peaks at 2.8, 3.9, and 4.3 V vs. Li/Li^+ (Fig. 8b). *Ex situ* X-ray absorption/emission spectroscopy identified the redox centers in the dQ/dV plot: Mn^{4+}/Mn^{3+} redox couple for the peaks at 2.8 V, $Ni^{4+}/Ni^{3+}/Ni^{2+}$ redox couple for the peaks at 3.9 V, and oxygen reduction for the peaks at 4.3 and 3.3 V vs. Li/Li^+ (Fig. 9). Especially, Curie constant (C) was almost constant from 3.6 to 3.1 V vs. Li/Li^+ during discharge, implying the reduction of the diamagnetic O_2^{2-} ($S = 0$) to diamagnetic O_2^- ($S = 0$) (Fig. 10).

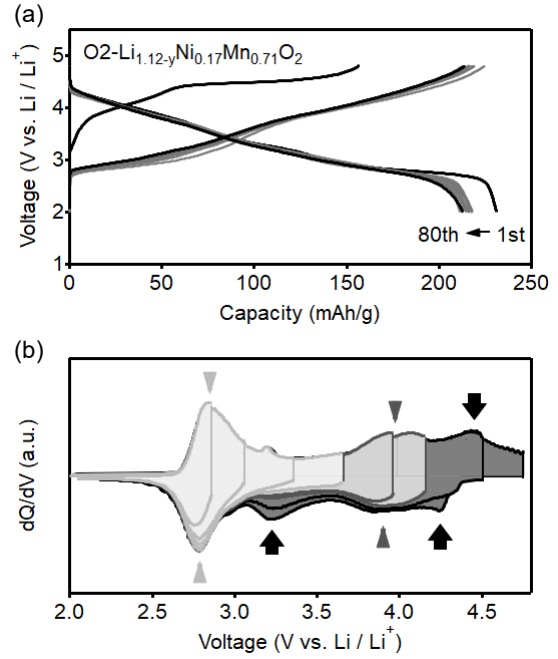


Fig. 8 (a) Galvanostatic charge/discharge curves, (b) dQ/dV plots with incremental cutoff voltages of O2-type $Li_{1.12-y}Ni_{0.17}Mn_{0.71}O_2$ in LIBs.

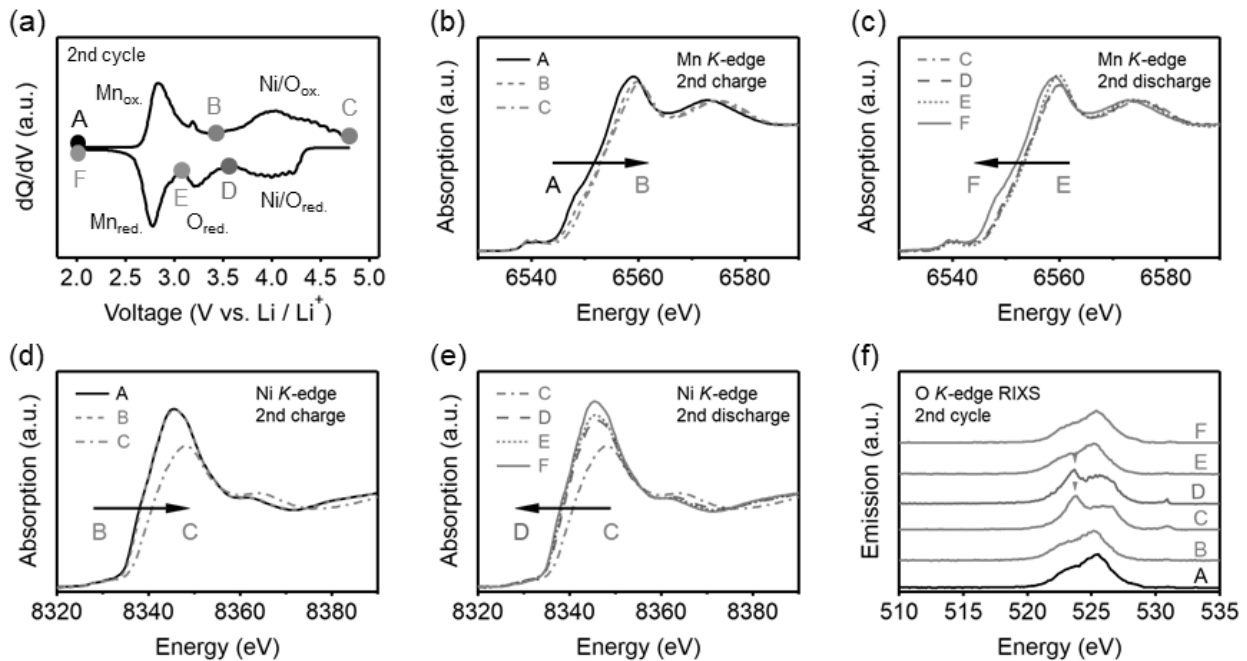
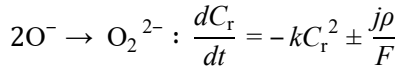


Fig. 9 Identification of redox couples upon the second charge/discharge process; (a) the dQ/dV curve, (b, c) Mn K-edge X-ray absorption spectroscopy (XAS), (d, e) Ni K-edge XAS and (f) O K-edge Resonance Inelastic X-ray Scattering (RIXS) spectra.

To quantify the competition between O^- and O_2^{2-} , DFT calculations were conducted where the model structures of O_2 -type $Li_{14/12-x}Ni_{2/12}Mn_{8/12}O_2$ are obtained using the genetic algorithm. Oxygen atoms near Li defects in transition-metal layers are strongly oxidized compared to the others. Dimerization energy $\Delta_f E$ is negative at the end of delithiation, suggesting the thermodynamically favorable O_2^{2-} formation (Fig. 11). In addition, $\Delta_f E$ of peroxo-like dimers near Ni are lower than that near only Mn.

The electronic structure is analyzed by COOP approach. Before dimerization ($x = 0.83$), bonding/antibonding π -type interactions between O $2p$ and Mn/Ni t_{2g} states are found far below and above the Fermi level, which stabilizes the localized hole in nonbonding O $2p$ orbitals through strong π back-donation.¹⁸ After dimerization ($x = 1.17$), σ/σ^* and π/π^* molecular orbitals, which consisted of O $2p$ orbitals, were clearly confirmed around O–O dimers. Integrated COOP value (iCOOP) between O_2^{2-} and Ni is smaller than that between O_2^{2-} and Mn, whereas iCOOP between O–O bond near Ni is larger than that near only Mn. These results indicate that the weak interaction between peroxo-like dimers and Ni facilitates the dimerization.

Finally, kinetics of dimerization is investigated based on the simple second-order reaction as follows:



where C_r is a concentration of O^- , k is a rate constant, j is a current density, ρ is a density of electrode material, and F is the Faraday constant. The discharge capacity Q for $O_2^{2-} \rightarrow O_2^{4-}$ as a function of constant-voltage duration Δt after oxygen oxidation is calculated as

$$Q(\Delta t) = jt_1 - \frac{F}{\rho} \frac{1}{\frac{1}{C_r(t_1)} + k\Delta t}$$

where t_1 is time for oxygen oxidation upon charging. $Q(\Delta t)$ is obtained by Gaussian fitting to the reduction peak at 3.3 V vs. Li/Li⁺ in the dQ/dV plots after keeping cell voltage at 4.8 V vs. Li/Li⁺ for Δt . A plot of $Q(\Delta t)$ vs. Δt provides the rate constant $k = 3.5 \times 10^{-2} [\text{cm}^3 \text{mol}^{-1} \text{s}^{-1}]$ (Fig. 12).

Conclusive square scheme is summarized in Fig. 13. The chemical state at the end of charge is estimated as $O_2-Li_{1.12-y}Ni_{0.17}Mn_{0.71}O_{1.75}(O^-)_{0.13}(O_2^{2-})_{0.06}$ where 12.5% of oxide ions (0.25 oxide ions per two oxide ions) are oxidized and 48% oxidized oxide ions (0.12 oxide ions per 0.25 oxidized oxide ions) undergo the dimerization.

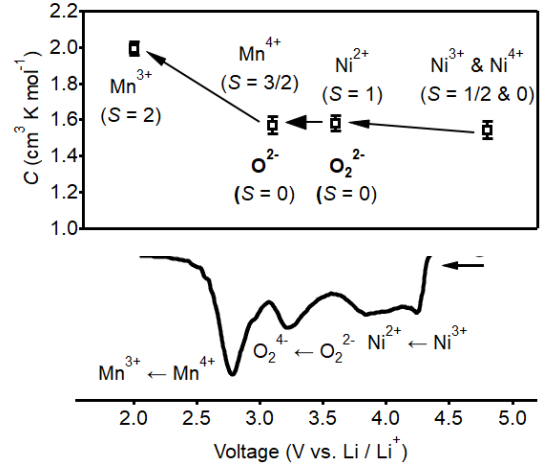


Fig. 10 Curie constants (C) of $O_2-Li_{1.12-y}Ni_{0.17}Mn_{0.71}O_2$ and the dQ/dV plot for discharge.

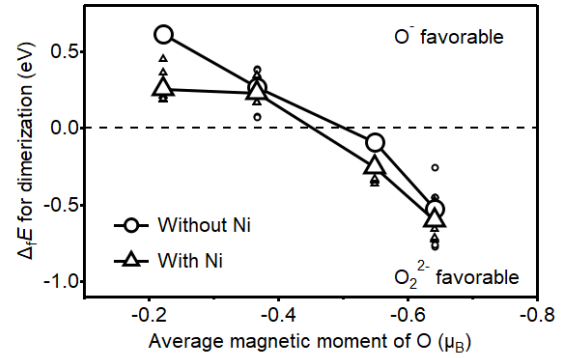


Fig. 11 Peroxo-like dimer formation energy at the end of delithiation against average magnetic moment of O.

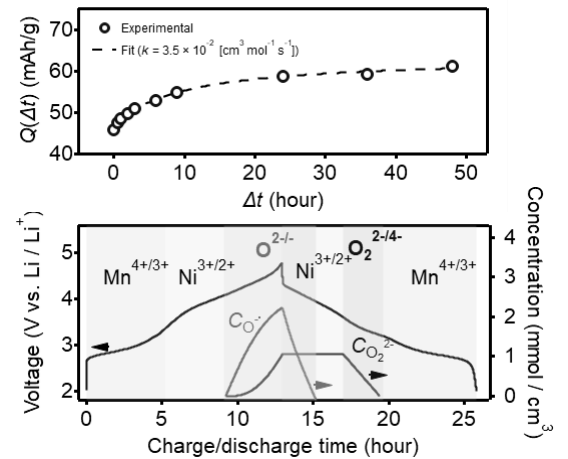


Fig. 12 Time dependence of the discharge capacity for $O_2^{2-} \rightarrow O_2^{4-}$ reduction and the concentrations of O^- and O_2^{2-} in $O_2-Li_{1.12-y}Mn_{0.71}Ni_{0.17}O_2$.

4. Conclusion

In this thesis, the improvements of material cost and energy density for rechargeable batteries are approached by exploring cathode materials (Fig. 14). (i) To reduce material costs, SIB is a possible alternative for LIB because of more abundance of sodium resource than lithium, whereas development of high-voltage cathode materials is crucial to compensate for the inherently higher redox potential of Na/Na⁺ couple than that of Li/Li⁺ couple. Exploration and reaction mechanism analysis suggest that phosphate-based compounds using low-cost Cr as the redox center instead of high-cost Co and Ni is a promising class of high-voltage cathode materials for SIBs. (ii) Oxygen redox chemistry is of great interest for increasing a capacity of cathode. Utilizing the structural integrity of O₂-type layered oxides against oxygen-redox reactions, peroxide ion O₂²⁻ formation is identified as the origin of large voltage hysteresis for oxygen-redox reactions. Ni facilitate the formation of peroxo-like dimers compared to Mn, while O⁻ radical species is favorable to peroxo-like O₂²⁻ at the early state of oxygen oxidation. The composition of transition-metal ions and the degree of oxygen oxidation play a critical role in realizing high-voltage operation of oxygen-redox cathode. These findings will pave the way toward the development of high energy density cathode materials for next-generation rechargeable batteries.

~ References ~

- [1] A. K. Padhi, *et al.*, *J. Electrochem. Soc.* **1997**, *144*, 2581–2586.
- [2] C. Masquelier, *et al.*, *Chem. Rev.* **2013**, *113*, 6552–6591.
- [3] M. Nose, *et al.*, *J. Power Sources* **2013**, *234*, 175–179.
- [4] H. Zhang, *et al.*, *NPG Asia Mater.* **2017**, *9*, e370.
- [5] G. Hautier, *et al.*, *Chem. Mater.* **2011**, *23*, 3495–3508.
- [6] M. Herklotz, *et al.*, *Electrochim. Acta* **2014**, *139*, 356–364.
- [7] U. Opik, *et al.*, *Proc. Roy. Soc.* **1957**, *238*, 425–447.
- [8] A. Urban, *et al.*, *Phys. Rev. Lett.* **2017**, *119*, 1–6.
- [9] O. Mustonen, *et al.*, *Phys. Rev. B* **2016**, *93*, 014405.
- [10] K. Luo, *et al.*, *Nat. Chem.* **2016**, *8*, 684–691.
- [11] D.-H. Seo *et al.*, *Nat. Chem.* **2016**, *8*, 692–697.
- [12] E. McCalla, *et al.*, *Science*, **2015**, *350*, 1516–1521.
- [13] M. Sathiya, *et al.*, *Nat. Mater.* **2015**, *14*, 230–238.
- [14] W. E. Gent, *et al.*, *Joule* **2020**, *4*, 1369–1397.
- [15] B. Xu, *et al.*, *Energy Environ. Sci.* **2011**, *4*, 2223–2233.
- [16] N. Yabuuchi, *et al.*, *Adv. Energy Mater.* **2014**, *4*, 1301453.
- [17] D. Eum, *et al.*, *Nat. Mater.* **2020**, *19*, 419–427.
- [18] T. Sudayama, *et al.*, *Energy Environ. Sci.* **2020**, *13*, 1492–1500.

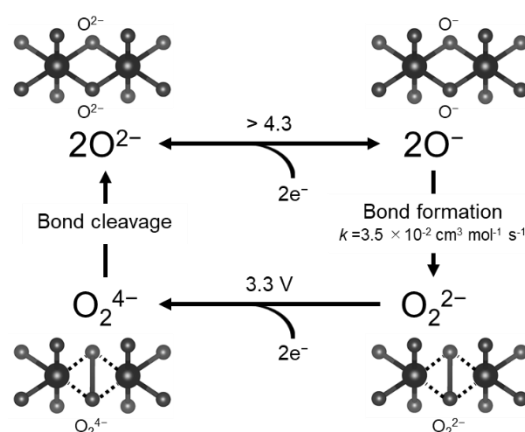


Fig. 13 Square scheme of oxygen-redox reaction.

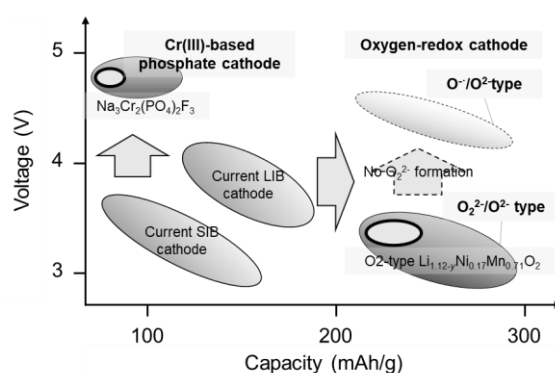


Fig. 14 Achievements of this thesis (areas with orange and blue bold line) in the field of cathode materials for rechargeable batteries.